The effect of the geometry and material properties of a carbon joint produced by electron beam induced deposition on the electrical resistance of a multiwalled carbon nanotube-to-metal contact interface

2010 Nanotechnology 21 035202

(http://iopscience.iop.org/0957-4484/21/3/035202)

Nanotechnology **21** (2010) 035202 (12pp) doi:10.1088/0957-4484/21/3/035202

The effect of the geometry and material properties of a carbon joint produced by electron beam induced deposition on the electrical resistance of a multiwalled carbon nanotube-to-metal contact interface

Konrad Rykaczewski[1], Matthew R Henry[1], Song-Kil Kim[1], Andrei G Fedorov[1,4], Dhaval Kulkarni[2,3], Srikanth Singamaneni[2,3] and Vladimir V Tsukruk[2,3]

[1] Woodruff School of Mechanical Engineering, Georgia Institute of Technology, Atlanta, GA 30332, USA
[2] School of Materials Science and Engineering, Georgia Institute of Technology, Atlanta, GA-30332, USA
[3] School of Polymer, Textile and Fiber Engineering, Georgia Institute of Technology, Atlanta, GA-30332, USA

E-mail: andrei.fedorov@me.gatech.edu

Received 2 October 2009, in final form 18 November 2009
Published 7 December 2009
Online at stacks.iop.org/Nano/21/035202

Abstract
Multiwall carbon nanotubes (MWNTs) are promising candidates for yielding next generation electrical and electronic devices such as interconnects and tips for conductive force microscopy. One of the main challenges in MWNT implementation in such devices is the high contact resistance of the MWNT–metal electrode interface. Electron beam induced deposition (EBID) of an amorphous carbon interface has previously been demonstrated to simultaneously lower the electrical contact resistance and improve the mechanical characteristics of the MWNT–electrode connection. In this work, we investigate the influence of process parameters, such as the electron beam energy, current, geometry, and deposition time, on the EBID-made carbon joint geometry and electrical contact resistance. The influence of the composition of the deposited material on its resistivity is also investigated. The relative importance of each component of the contact resistance and the limiting factor of the overall electrical resistance of a MWNT-based interconnect is determined through a combination of a model analysis and comprehensive experiments.

(Some figures in this article are in colour only in the electronic version)

1. Introduction

As the feature sizes in electronic devices decrease to nano-scale, metal resistivity increases due to surface and grain boundary scattering and wire type structures become more vulnerable to electromigration effects [19, 33]. Multiwall carbon nanotubes' (MWNTs) ballistic transport characteristics, high carrier mobility in the diffusive region, capability of handling large current densities without mechanical degradation, and exceptional mechanical properties make them an attractive material for nano-electronic components [16, 2, 20]. Close *et al* [13] recently demonstrated GHz range operation of an

[4] Author to whom any correspondence should be addressed.

integrated circuit with MWNT interconnects. However, the effective resistivity of the MWNT-based interconnect was two orders of magnitude higher than that of copper. This example highlights one of the main challenges in implementation of MWNT as electrical components, namely the high ($\sim 10^4$–10^8 Ω) contact resistance of the MWNT–metal conductor connection [46, 16]. In the case of MWNT components, establishment of electrical connection with inner shells of the tube poses an additional challenge [18].

While several groups were able to demonstrate the low contact resistance in vertically aligned [34, 39] or free standing MWNT [18, 28], the methods utilized, such as 'dipping' the ends of MWNTs into a liquid metal [18] or growing MWNTs from preformed catalyst nanoparticles, do not allow for control over the orientation of the tube and are difficult to implement in on-the-substrate interconnect configuration. In this type of device geometry, methods such as electron beam lithography (EBL) of metal pads [26], joule heating [16], and gold nanoparticle ('nano-ink') suspensions deposition [15] have been applied to lowering of the contact resistance. However, these methods produce side-contacted rather than end-contacted CNT–metal geometries, which according to Tersoff [46] result in a weak electronic coupling at the Fermi surfaces and thus a higher intrinsic contact resistance.

Application of electron beam induced deposition (EBID) of carbon [4, 38, 10] or metal [32, 9] to make the contact to the MWNT has been demonstrated to simultaneously reduce the electrical contact resistance [4] and to improve mechanical characteristics of the connection [14]. Since Bachtold *et al* [4] demonstrated that high resolution electron beam imaging of MWNT significantly lowers its electrical contact resistance to the substrate, numerous groups [38, 10, 3, 23, 50] have followed this simple approach. The accelerating voltages and currents used varied from 5 kV and 7 pA [38] to 20 kV [4] and 100 pA [14], respectively. The characterization of the EBID-made amorphous carbon interface has been limited to electrical [38, 4, 3, 29, 31, 32, 42, 43] and structural (TEM imaging [23, 5]). In this work, we investigate the influence of EBID process parameters, such as electron beam energy, current, geometry, thermal treatment, and deposition time on the EBID-made carbon connection geometry and resistance. The relative importance of each component in the resistance chain and the limiting factor defining the bottleneck in the total resistance of a MWNT-based interconnect is determined using a simple analysis and supporting EBID experiments.

2. MWNT interconnect resistance

Yoshikawa *et al* [50] determined that while the EBID-made carbon interface consists of a tunneling and Ohmic resistance, at room temperature and above the tunneling resistance can be neglected. Thus, the total measured resistance of a MWNT interconnect is equal to the sum of the individual resistances of components connected in series, as shown in figure 1. According to Slade [41] the electrical contact resistance, R_{contact}, is equal to the sum of the constriction resistance and interfacial film resistance. In case of a MWNT interconnect connected to the metal pad/electrode via an amorphous carbon joint, two interfacial films contribute to the contact resistance: at the amorphous carbon joint–MWNT interface ($R_{\text{aC–MWNT interface}}$) and at the amorphous carbon joint–metal electrode interface ($R_{\text{aC–metal interface}}$). If the joints at both ends of the MWNT are assumed to be identical, the total resistance of a MWNT interconnect, R_{total}, equals to:

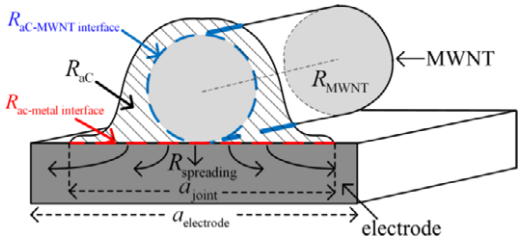

Figure 1. Schematic representation of the components contributing to the total resistance of a MWNT interconnect.

$$R_{\text{total}} = 2R_{\text{aC–MWNT interface}} + 2R_{\text{aC}} + 2R_{\text{aC–metal interface}} + 2R_{\text{spreading}} + R_{\text{MWNT}}. \quad (1)$$

Here R_{aC} is the constriction resistance of the amorphous carbon joint itself, $R_{\text{spreading}}$ is the spreading resistance of the metal electrode (on a SiO_2/Si deposition substrate), and R_{MWNT} is the resistance of the MWNT. The location of each of the components contributing to R_{total} is schematically shown in figure 1.

Without loss of generality, if the joint is assumed to have a circular base area, $R_{\text{spreading}}$ can be estimated using an expression derived by Kennedy [24]:

$$R_{\text{spreading}} = \frac{\rho_{\text{metal}} H}{\pi a_{\text{joint}}}. \quad (2)$$

Here, ρ_{metal} is the resistivity of the electrode metal, a_{joint} is the diameter of the base (contact) area, and H is the spreading resistance factor. The spreading resistance factor is a function of the lateral dimension of the base area (radius a_{joint}, if a disk shape is assumed, and its thickness h) and a representative length scale ($a_{\text{electrode}}$) of the metal electrode (figure 1). The representative dimensions $a_{\text{joint}} = 10$ nm, $h = 200$ nm, and $a_{\text{electrode}} = 2500$ nm yield $H \sim 3$. If the electrode with above specified dimensions is made of copper, the spreading resistance is equal to 0.6 Ω and can be neglected.

The electrical resistance of a circular interfacial films is equal to [6]:

$$R_{\text{interface}} = \frac{\sigma}{\pi a_{\text{joint}}^2} \quad (3)$$

where σ is equal to the product of the layer resistivity and thickness and is assumed to be constant. The bulk electrical resistance of the carbon joint, R_{ac}, depends on the specific geometry of the joint,

$$R_{\text{aC}} \sim \frac{\rho_{\text{aC}} l_{\text{s}}}{A_{\text{s}}} \quad (4)$$

where ρ_{aC} is the bulk resistivity of the carbon, l_{s} and A_{s} are the representative length and cross-sectional area of the joint, with their ratio equal to an inverse of the representative

length scale of the deposit, L_{ac}. The electrical resistance of a MWNT depends on the number of defects in the structure of the tube, its length, the number of conducting shells and their diameter [27]. The resistance of a single shell is given by [27]:

$$R_{\text{shell}} = \frac{h}{2e^2 N}\left(1 + \frac{L_{\text{MWNT}}}{\lambda}\right) \tag{5}$$

where $h/2e^2$ is the quantum resistance which equals to 12.9 kΩ, and L_{MWNT}, λ, and N are the length of the tube, the mean free path of an electron, and the number of conduction channels in the shell, respectively. The number of conducting channels depends on the tube diameter, D, and for $D > 3$ nm can be approximated as [27]:

$$N_{\text{shell}}(D) \approx aD + b \tag{6}$$

where $a = 0.0612\ \text{nm}^{-1}$ and $b = 0.425$. An error introduced by the above equation due to different chirality of tubes is within 15% for all values of D. For both metallic [22] and semiconducting [27] shells of the MWNT, the electron mean free path depends linearly on the diameter of the tube and can be approximated as $\lambda \sim 1000D$ (with D in nm) [27]. Thus, a MWNT with diameter of 100 nm, length ∼1 μm, and only the outer shell conducting should have a resistance of ∼2 kΩ. Conduction through multiple shells significantly lowers the total resistance of the tube, and would be ultimately desired for MWNT interconnect applications.

As made, a typical ∼5 μm MWNT interconnect has a total resistance on the order of a few to few hundred MΩ, while MWNT has a resistance of a few kΩ. Thus, initially the resistance of the carbon nanotube itself is negligible in comparison to the total resistance of the interconnect. Further, without loss of generality if one assumes the contact resistance of one of the ends to be much smaller than the other (for example if one of two ends already has a good connection established using EBID), equation (1) reduces to:

$$\begin{aligned} R_{\text{total}} &\approx R_{\text{contact}} \approx R_{\text{aC-MWNTinterface}} + R_{\text{aC}} + R_{\text{aC-metal interface}} \\ &\approx \frac{\rho_{\text{aC}}}{L_{\text{aC}}} + \frac{\sigma_{\text{aC-metal}}}{L^2_{\text{aC-metal}}} + \frac{\sigma_{\text{aC-MWNT}}}{L^2_{\text{aC-MWNT}}} \end{aligned} \tag{7}$$

where $L_{\text{aC-metal}}$ and $L_{\text{aC-MWNT}}$ are the length scales for the carbon joint–metal and carbon joint–MWNT interfaces, respectively.

3. Experiment

MWNTs with diameters of 50–150 are purchased from a commercial vendor, purified by refluxing in nitric acid for 48 h, and dispersed by ultrasonication in dimethylformamide (DMF). Individual MWNTs are aligned between two ∼200 nm thick chrome electrodes on top of a ∼1 μm SiO_2 layer on a Si wafer using dielectrophoresis [42]. Specifically, the following procedure is used: a small drop of DMF solution containing MWNTs (MWNT concentration 1–10 $\mu g\ ml^{-1}$) is placed atop of metal electrodes (electrode separation 1–5 μm), and an AC voltage signal is applied with frequency of 5 MHz and peak-to-peak voltage of 1–10 V for a period of 1 min. After dielectrophoretic alignment, the residual droplet is removed by air brush to avoid excessive nanotube clustering between the electrodes and the sample is transferred to ESEM for EBID experiments. EBID carbon joints are fabricated using Quanta 200 ESEM with residual hydrocarbons as a precursor at the background (chamber) pressure of $\sim 10^{-5}$ Torr. The cone-shaped carbon joints are deposited by keeping the electron beam in spot mode for a period of 5 min. Electron beam energy in 20–30 keV range and electron beam current (spot size) in the 5–140 pA range are used for deposition. The square-shaped carbon deposits with dimensions of ∼300 nm × 300 nm are made by scanning the electron beam with energy of 25 keV and current of ∼140 pA at a frame time of 0.411 s and resolution of 2048 pixels × 1768 pixels for a period of ∼4–5 min, corresponding to a refresh time of 2.4 Hz and a pixel dwell time of 100 ns. The 2 μm long platinum EBID line is deposited by scanning the electron beam with energy of 25 keV and current of ∼140 pA with simultaneous injection of an $(CH_3)_3Pt(CpCH_3)$ organometallic precursor. The ESEM is operated in a line mode with resolution of 2048 pixels and the line time of 0.23 ms for 10 min, corresponding to a refresh time of 2.4 Hz and pixel dwell time of 100 ns.

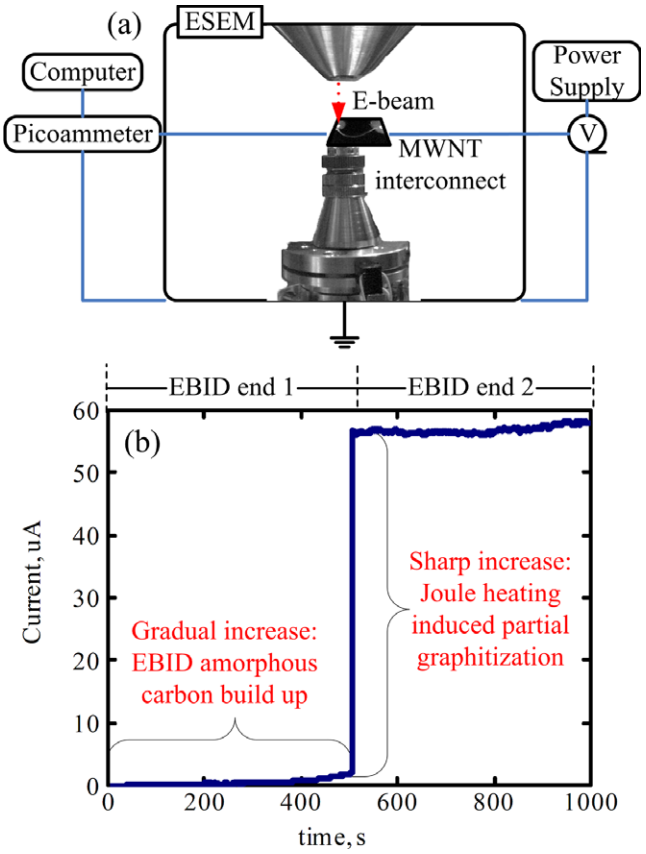

Figure 2. (a) Schematic of the modified FEI Quanta 200 used for *in situ* current measurements and (b) typical current versus time measurement of EBID amorphous carbon MWNT–electrode interface.

As shown in figure 2(a), the FEI Quanta 200 ESEM is modified so that a DC voltage signal can be applied between the electrodes on the substrate used for deposition, and the resulting current is measured using Keithley 6485

Picoammeter *in situ* during the operation. The electric current data are directly imported into Microsoft Excel using the ExcelLINK program for post-processing.

The electrical measurements are performed in two ways. In the first method, a desired input voltage is applied and the resulting current is recorded during the deposition process. This *in situ* approach has been previously used by Ando *et al* [3] and Madsen *et al* [29]. In the second method, a set of current versus voltage data is collected in vacuum, but with the electron beam turned off, i.e., in the post-deposition mode. To measure an evolution of the electrical resistance of the carbon joint as it grows, the procedure is repeated after each consecutive stage of the deposition process. Figure 2(b) shows a typical current versus time measurement for EBID carbon joint formation. The results obtained compare well to those of Ando *et al* [3] and Madsen *et al* [29]. In this case, EBID is performed at an accelerating voltage of 25 keV, spot size 3, high vacuum conditions ($\sim 10^{-5}$ Torr) and a fixed electrode DC bias of ~1.5 V. Biasing of substrate with low (~2–5 V) voltage does not significantly impact the electron scattering and generation process [11], but an induced increase in the surface temperature can significantly impact the surface diffusion coefficient, mean surface lifetime, and sticking coefficient of hydrocarbon precursor molecules, which are all important to dynamics of EBID growth [48]. Focusing the electron beam on small areas surrounding the ends of MWNT for 10–20 min gradually increases the measured current (corresponding to a gradual decrease in the contact resistance due to a build-up of the carbon deposit) and at some point a drastic drop in the measured resistance is observed. According to Banhart *et al* [5], Yoshikawa *et al* [50], and Kahng *et al* [23] this change can be attributed to the Joule-heating-induced partial or full graphitization of the deposited amorphous carbon associated with an increase in the electric current flowing through the nanotube due to the reduced resistance of growing carbon joints.

In order to deconvolute the change in resistance of the carbon joint due to geometrical factors and due to the properties of the deposited material, the *in situ* measurements are performed at a lower bias voltage. Before deposition experiments, the DC voltage difference between metal terminals connected by MWNT is adjusted to a baseline value V_0, so that the resulting current is on the order of few hundred picoamps so it is small enough to avoid a spontaneous joint graphitization during deposition. The V_0 value depends on the initial resistance of the MWNT interconnect and ranges from 0.05 to 2 V. Following the approach of Kahng *et al* [23] and Yokishiwa *et al* [50], the changes in the material properties due to Joule heating are studied after the deposition process. Specifically, the bias voltage across the interconnect is gradually increased until a sharp increase in the current, corresponding to the graphitization of the amorphous carbon, is observed.

The phase composition and the changes in the structure of the amorphous carbon due to annealing at different temperatures are studied using Raman spectroscopy. Raman measurements are performed using a Witec (Alpha 300R) confocal Raman microscope using Ar^+ ion laser (514.5 nm) as an excitation source according to the usual procedure [40]. The intensity of the excitation source was fixed at 1 mW. Raman imaging of the EBID-made carbon is performed using a resolution of 3 cm^{-1}. The imaging was performed at a resolution of 50 pixels × 50 pixels. The individual spectra used for analyzing the peak positions and other features are an average of more than 80 individual spectra.

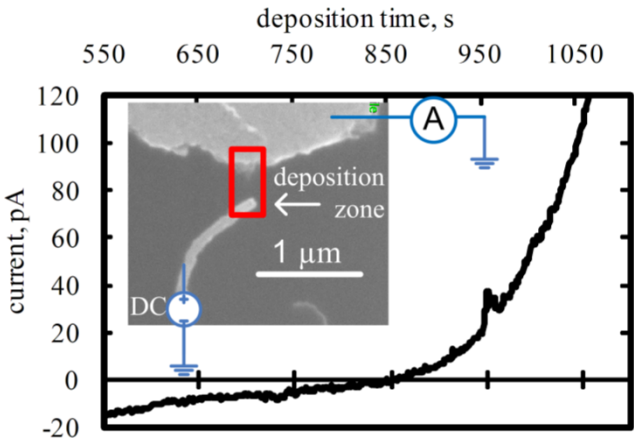

Figure 3. Current versus time measurement during electrode–MWNT gap bridging experiment. Inset shows the corresponding SEM image of the gap (the other end of the MWNT is connected to the second electrode). The electron beam current for this experiment was ~140 pA.

4. Results and discussion

4.1. Influence of electron beam on electrical measurements

Influence of the electron beam on *in situ* electrical measurements is an important factor that has to be taken into account in interpreting the electric current measurements. The electron beam contributes to the measured current in two ways. First, a fraction of the impinging primary electrons are scattered within a tube and add directly to the measured current. Second, the impinging primary electrons contribute indirectly to the measured current by generation of multiple secondary electrons during inelastic collisions within the material. In the next two sub-sections the extent to which the primary electrons alter the *in situ* current measurement is analyzed using experimental measurements.

4.1.1. Direct contribution of the primary electrons. Figure 3 shows the electrical current versus time measurement corresponding to the electrode–MWNT gap bridging deposition experiment shown in the inset. Initially, the measured current is negative and corresponds exactly to the number of primary electrons impinging on the substrate (beam current) minus the number of backscattered and secondary electrons [8]. As a metal-to-tube connection begins to form, the flow of electron from one electrode to the other increases due to an applied bias voltage and begins to dominate the current resulting from the impingement of primary electrons from the electron beam (seen as transient from negative to positive current past ~850 s in figure 3).

The current due to impingement of primary electrons is negative because the primary electrons penetrate through the thin insulator layer and are collected at the ground terminal (figure 3). However, the direct contribution of the primary electrons on the measured electrical current is on the order of the electron beam current (∼pA) and can be neglected when measuring much higher currents (∼nA–μA) generated upon applying an external DC bias voltage between metal terminals connected by MWNT.

4.1.2. Indirect contribution of the primary electrons. When it is scattered within a medium each primary electron undergoes multiple inelastic collisions in which low energy secondary electrons are generated. A small fraction of these generated secondary electrons emerge from the substrate. Without an external bias the rest of generated secondary electrons re-equilibrate within the substrate [8]. However, when an external bias is applied the generated electrons can migrate between the electrodes, contributing to the measured electric current [45]. Figure 4 shows the time evolution of measured current during consecutive stages of a deposition process, consisting of building a sequence of overlapping square-shaped carbon deposit blocks to bridge the gap between MWNT and the metal electrode (figure 3).

The measured current increases when the electron beam is turned on and decreases when the electron beam is turned off, with the characteristic sharp rise and slow exponential decay in time. As shown in figure 4, this behavior is repeatedly observed during multiple electron beam on/off cycles. When the electron beam is focused on the amorphous carbon bridging connection between the MWNT and a metal electrode (figure 4), the baseline current (the steady current value at the end of each decay cycle) gradually increases.

An increase in the current corresponds to a decrease in the resistance of the bridge due to the extra amorphous carbon deposition. At the same time, the baseline current in figure 4(a) does not appreciably increase because the deposition occurs on top of the already low resistance MWNT. The current versus time evolution is also studied during deposition of a platinum line between two metal electrodes with constant electric potential bias applied along the line. The electron beam is turned on during the deposit growth process, and then intermittently turned on and off while focusing on different regions of the deposited line (the on/off beam cycling is done when Pt-containing precursor is no longer supplied into the chamber of the SEM). As shown in figure 5(a), the electric current increases during the growth of the line and decays exponentially when the beam is turned off. As shown in figure 5(b), the baseline current increases only when the electron beam is focused on a platinum line. As in the bridging gap experiment, the increase in the baseline current can be attributed to lowering the resistance of the conducting line due to extra material (Pt) deposition. Similar experimental trends have been recently observed by Porrati *et al* [35], who attributed the exponential decay of the current, when an electron beam is turned off, to migration of the extra injected primary electrons towards the electrode. However, the Porrati's hypothesis cannot explain the above experiments because the

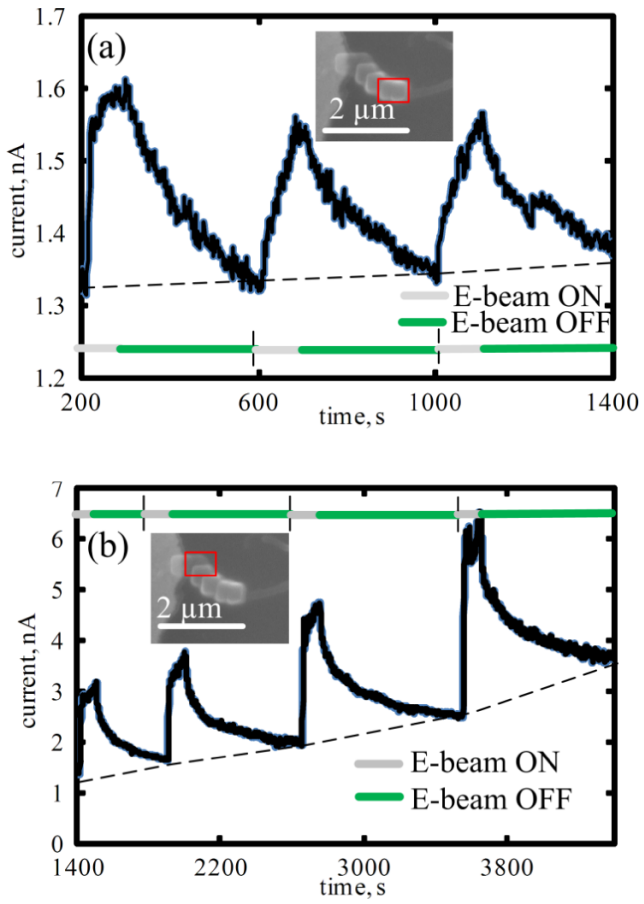

Figure 4. Current versus time for consecutive stages of a deposition process consisting of building a sequence of square carbon deposits bridging the gap between MWNT and the metal electrode. Regions exposed to the electron beam are marked in SEM images in insets (a) and (b). The dashed line traces the baseline (DC) current, which drifts over time in the course of deposition process. The electron beam current for this experiment was ∼140 pA.

current due to the injected primary electrons is several orders of magnitude lower than the measured current. On the other hand, each primary electron undergoes multiple inelastic collisions and produces multiple low energy electrons. For example, a primary electron with energy of 25 keV scattered within silicon substrate has a penetration depth of ∼6 μm and can undergo several hundred collisions generating secondary (low energy) electrons before losing all its energy. Indeed, the magnitude of the observed decay current suggests that it is due to mostly the generated, not primary, electrons. To explain the long exponential time decay it can be noted that the EBID-deposited material and the SiO_2 layer act as the capacitors storing the charge. The capacitive element is charged during electron injection (the beam in on) and slowly discharges when the beam is turned off, providing a transient capacitor-like current rise and decay over the baseline DC current, which increases due to a gradual deposit build-up and associated reduction in the resistance.

Irrespective of the physical mechanism responsible for transient changes in measured current, *in situ* current measurements cannot be used for quantitative determination

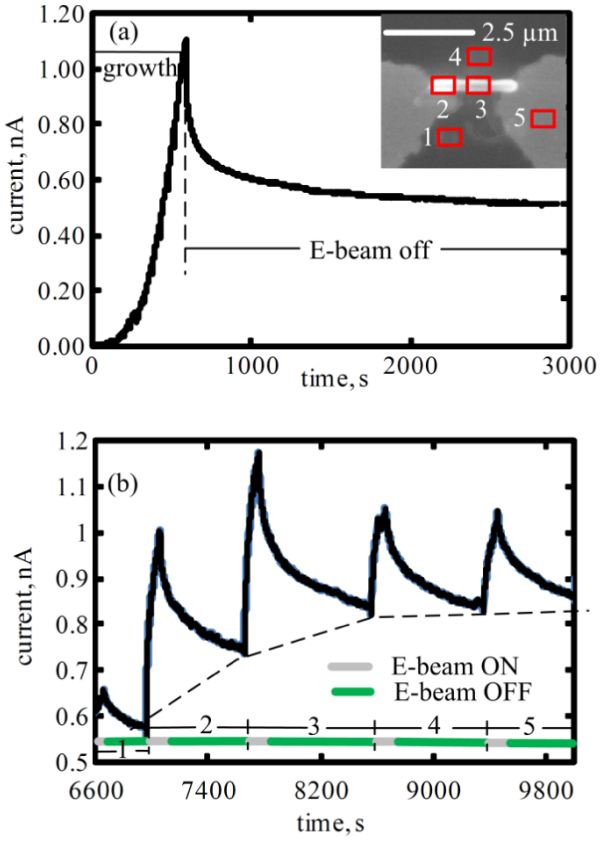

Figure 5. (a) Current versus time measurement for platinum line deposition experiment, (b) current versus time resulting from turning the electron beam on and off in various regions on and around the platinum line. Regions exposed to the electron beam are marked in SEM image in insets in (a). The dashed line shows the trace of the baseline (DC) current. The electron beam current for this experiment was ∼140 pA.

of changes in the MWNT interconnect resistance. The *in situ* current trends can only be utilized as a qualitative measure of the relationship between EBID carbon deposit and the resistance of the formed joint between MWNT and a metal pad. To avoid measurement distortion, quantitative resistance measurements must be taken before and after each deposition step. Specifically, the DC current versus voltage data are taken at least ∼10 min after the electron beam is turned off, allowing the measured current to reach its steady-state value.

4.2. Cone-shaped carbon joint deposition experiments

The change in MWNT interconnect resistance due to deposition of conical amorphous carbon joints is investigated. Figure 6 shows typical *in situ* current and step-wise resistance measurements, and the corresponding top view SEM images of the carbon joints (the entire interconnects are shown in figures 6(d) and (e)). As demonstrated in figure 6(a), the *in situ* measured current scales linearly with the deposit diameter. The trend is quantitatively confirmed by the fact that the total resistance of an interconnect scales linearly with the inverse of the diameter of the deposit (figure 6(b)).

The effect of the electron beam energy and current is also investigated. In each case the experiments are performed on

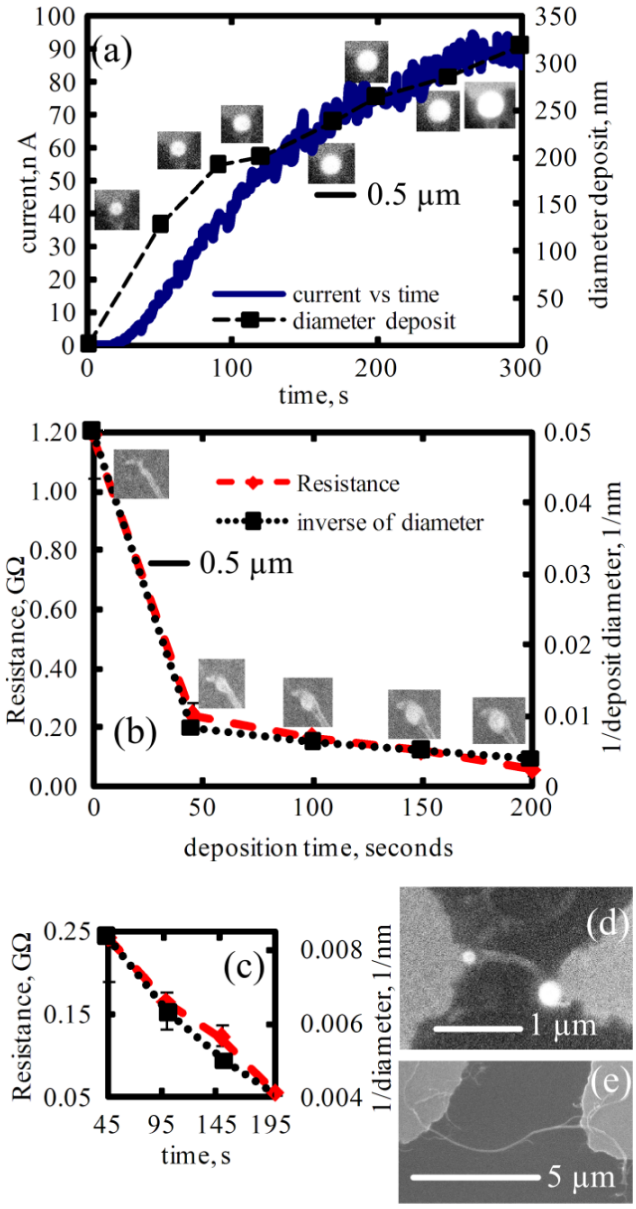

Figure 6. (a) *In situ* current versus time measurements during deposition on the left end of the interconnect shown in (d). (b) Resistance of a MWNT interconnect versus total deposition time for deposition on the left end of the interconnect shown in (e). (c) Detailed view during the later stages of the deposition process (the resistance measurements were taken ∼10 min after the end of each deposition stage. The SEM images showing the carbon joint at different stages of the deposition process are given in the inset in (a) and (b)).

MWNT with diameter of ∼50–100 nm for total deposition time of 5 min. The time necessary for the current to reach 90% of its value 5 min into the deposition process, $t_{90\%}$, is used as a comparison measure for different EBID settings. Figures 6(a) and (b) show the dependence of $t_{90\%}$ on energy and current of the electron beam, respectively. While the value of $t_{90\%}$ does not depend on the electron beam energy for electron beam energy in 20–30 keV range, it shows strong dependence on the electron beam current (spot size) in the 5–140 pA range. Specifically, the value of $t_{90\%}$ decreases from ∼275 to ∼50 s with the corresponding current increase from ∼5 to ∼140 pA.

The trends in figures 6(a) and (b) can be explained by the dependence of the time evolution of the deposit diameter on the electron beam settings. As shown in figure 7(c), the diameter of deposits formed at the spot size 3 and varied electron beam energies does not differ significantly for corresponding deposition times. In contrast, the diameter of deposits formed with the beam energy of 25 keV is much different for the early deposition times. Specifically, the diameter of the deposit formed after 1 min of deposition at 25 keV and the spot size 2 is much smaller than a corresponding diameter of a deposit formed at 25 keV and the spot size 4. However, after 5 min into the deposition process, diameters of the deposits formed at those two different settings are similar. Thus, the diameter of deposits formed at a lower beam spot size (corresponding to the lower beam currents) increases steadily with time, while the diameter of deposits formed at higher spot sizes (corresponding to the lower beam currents) increase rapidly but then saturates. Accordingly, the resistance of the deposits formed at low electron beam spot size decreases steadily, resulting in a long settling time $t_{90\%}$. The resistance of deposits formed at high spot sizes decreases rapidly and saturates, resulting in a short settling time $t_{90\%}$.

4.3. Multiple square carbon block deposition experiments

The results obtained in the preceding section demonstrate a direct dependence of the contact resistance on the carbon joint geometry. However, the relation between different structural components contributing to the total resistance of the MWNT interconnect (see figure 1) cannot be inferred from the experiments reported previously, because the volume of the amorphous carbon joint, the carbon joint-to-metal and the carbon joint-to-MWNT interfacial areas all increase at the same rate during the deposition process. Thus, following the relationship in equation (7), a decrease in the total resistance of the MWNT interconnect cannot be unambiguously attributed to any individual component in the chain of resistances that make up the total resistance.

The change in MWNT interconnect resistance due to deposition of multiple square-shaped amorphous carbon blocks in different locations on the MWNT end is investigated to define the dominant resistance in equation (1). Figure 8 shows typical *in situ* current and resistance measurements and the corresponding top view SEM images of the carbon joints. In both cases the first square block deposit (labeled '1' in figure 8) is made at the end of the MWNT, and the following three square blocks (labeled '2', '3', and '4' in figure 8) are deposited on the electrode without making direct contact to the MWNT. The fifth square block (labeled '5' in figure 8) is deposited on the part of the MWNT resting on top of the insulator (SiO_2) layer. The continuity of the deposit sequence is assured by a slight overlap of adjacent square blocks. The *in situ* measured current increases only during the deposition of the first and second square blocks (figure 8(a)), resulting in a respective resistance decrease in figure 8(b). A further increase in the deposit size or contact area of deposited carbon to the electrode or MWNT does not decrease the total resistance of the MWNT interconnect. The geometrical

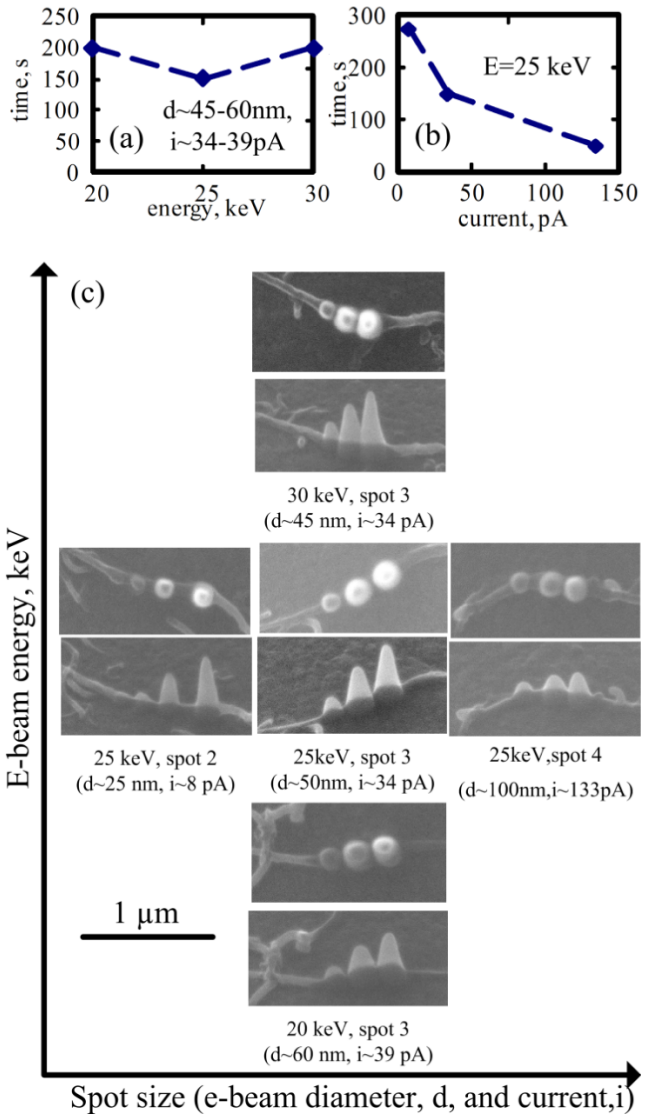

Figure 7. The time necessary for the current to reach 90% of its final value during 5 min deposition experiment in spot mode as a function of (a) electron beam energy and (b) electron beam current (spot size), (c) top view and 45°-angle view of cone-shape deposits on MWNT formed after 1, 3, and 5 min of deposition with settings corresponding to those in (a) and (b).

arrangement of the individual square block deposits does not impact the results, either. As shown in figure 8(c), the square deposits are grown in a straight line and to both sides of the MWNT. Depositing the second, third, and fourth carbon blocks increases only the length $\sim L_{aC}$ and area $\sim L^2_{aC-metal}$ in equation (7) (these two terms increase at the same rate since the carbon square blocks are thin). During the deposition of the fifth square block only the contact area of the amorphous carbon-to-MWNT interfacial film increases ($\sim L^2_{aC-MWNT}$). Since the measured resistance does not change during the deposition of the fifth square block, one can conclude that the area of the initial contact ($\sim L^2_{aC-MWNT}$) resulting from the deposition of the first square block is sufficient to decrease $R_{aC-MWNT\ interface}$ significantly below the value of the sum of R_{aC} and $R_{aC-metal\ interface}$. A decrease of the resistance

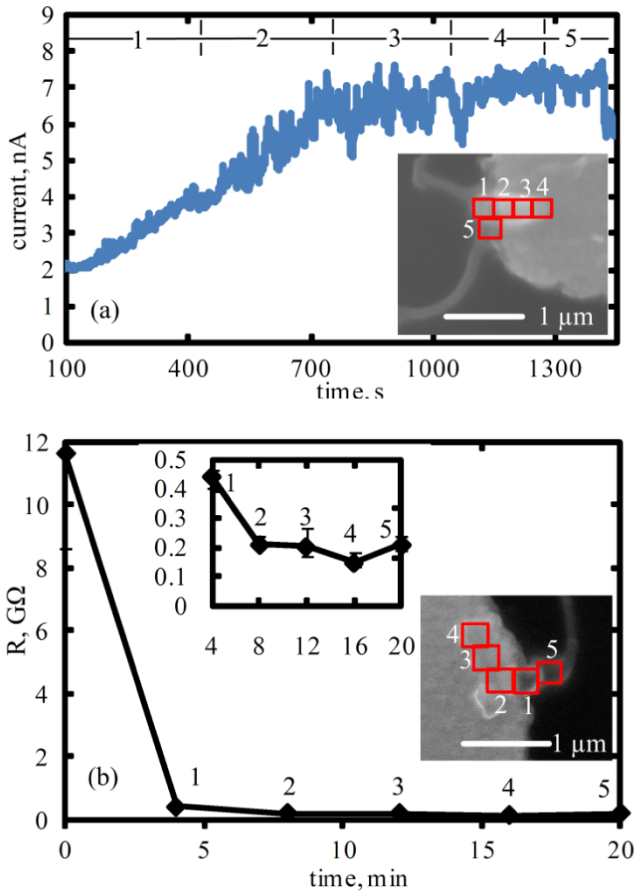

Figure 8. (a) *In situ* current versus time measurement during deposition at the MWNT end shown in the inset (b) total resistance of interconnect versus total deposition time for deposition at the MWNT end shown in the inset. The inset on the left shows a detailed view of resistance changes during the later stages of the deposition process (all resistance measurements are taken ∼10 min after the end of each deposition stage), and (c) different arrangements of the amorphous carbon connection consisting of multiple deposited carbon square blocks.

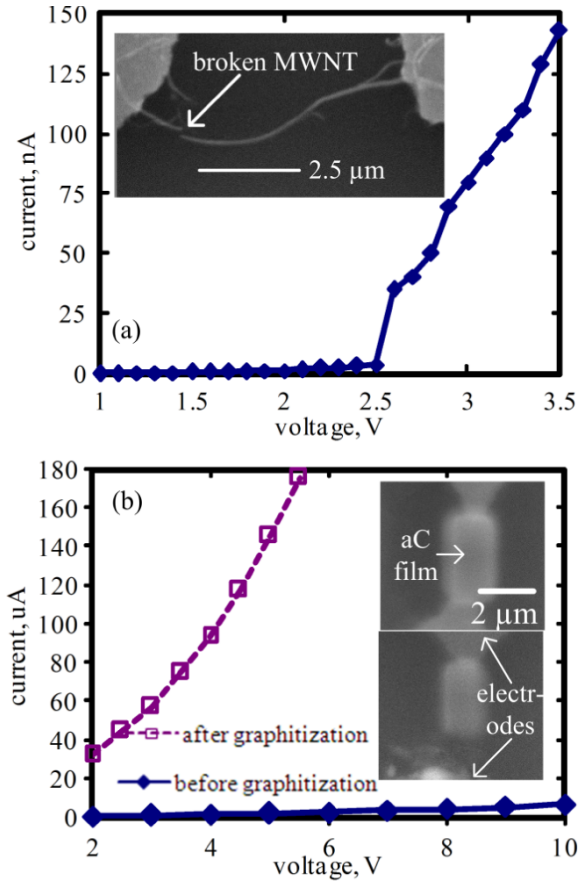

Figure 9. (a) Typical current versus voltage curve for a Joule-heating-induced partial graphitization of EBID-deposited carbon joints. Inset shows the MWNT after it became broken during the Joule heating experiment, and (b) before and after partial graphitization current versus voltage curves for carbon film grown using EBID of residual hydrocarbons. Insets show the film before graphitization and after its breakage due to high current passage.

during deposition of the second square block is due to further decrease in the values of R_{aC} and $R_{aC-metal\ interface}$. Saturation of the measured resistance during deposition of the third and fourth square blocks suggests that the resistance could not be decreased by further increase in L_{aC} and $L^2_{aC-metal}$.

In summary, these results show that for EBID-made carbon joints $R_{aC-MWNTinterface} \ll (R_{aC} + R_{aC-metalinterface})$, and in order to establish an effective Ohmic contact between the MWNT and a metal electrode, a much smaller contact area between the amorphous carbon deposit and the MWNT is required as compared to that between the amorphous carbon deposit and the metal electrode.

4.4. Joule-heating-induced partial graphitization of the carbon joint

A typical current versus voltage curve for Joule-heating-induced graphitization of the EBID-made amorphous carbon joint forming a connection to the MWNT interconnect is shown in figure 9(a). A drastic increase in the current is observed when the voltage is increased to 2.5 V. Exact measurement of the post-graphitization resistance is difficult because MWNT tend to burn out (i.e., physically destroyed) during the amorphous-to-crystalline phase transition of the carbon joint. The inset in figure 9(a) shows the MWNT

interconnect from figure 6 after it became broken during graphitization.

The change in the resistivity of the amorphous carbon deposit due to Joule heating is investigated. Amorphous carbon film is grown between two electrodes and partially graphitized in the same manner as the carbon joints to the MWNT interconnects described in preceding sections. The before and after graphitization current versus voltage curves and the corresponding SEM images of EBID carbon film are shown in figure 9(b).

Before graphitization and after graphitization resistances of the film are estimated from the slopes of linear parts of the current versus voltage data. The film resistance decreases from ∼2 to ∼0.05 MΩ, which corresponds to a resistivity decrease from 2×10^5 to 5×10^3 Ω μm. It should be noted that the resistivity of the partially graphitized film is still ∼1–2 orders of magnitude higher than that of bulk graphite [37]. The initial resistivity of the EBID carbon highly depends on the nature of residual hydrocarbons used as a precursor and reported values vary significantly [30]. Full graphitization of the film is difficult to achieve because of severe degradation of the film with an increased Joule heating (see lower inset in figure 9(b)).

4.5. Phase composition using Raman microscopy

To further understand the phase composition of the EBID-made carbon joints is investigated using Raman spectroscopy. Raman spectroscopy is powerful analytical technique for probing the physical and chemical properties of various carbon nanostructures such as carbon nanotubes, graphene, electron beam deposits [7]. Diameter and the electronic state (metallic versus semiconducting) dependence of radial breathing mode, strain sensitivity of graphitic band (G band) and the second harmonic of disorder band (G′ band) are exploited to characterize carbon materials [36, 49, 1, 21, 25]. Of particular significance for the present study is the ratio of the areas under the disorder band (D band) and the graphitic band (D/G ratio), which quantifies the size of the degree of graphitization (size of microcrystalline regions and the phase composition (amorphous versus crystalline)) [47, 17, 44, 7]. Specifically, the influence of annealing at different temperatures on the EBID-made carbon is analyzed. Figure 10 shows the Raman micromapping of carbon square acquired by integrating intensity from 1500 to 1700 cm^{-1} and the corresponding SEM image. The Raman spectra (and the Gaussian fits) for carbon square annealed in air for 3 min at 100, 200, 300, and 400 °C, the area ratio for D and G bands are shown in figure 11. One can clearly distinguish the characteristic G band (1580 cm^{-1}) and D band (1350 cm^{-1}).

Two distinct trends associated with amorphous carbon graphitization can be deduced from these data. First the D/G band ratio decreases significantly with an increase of the film annealing temperature from 100 to 200 °C. Second the full width at half maximum (FWHM) of the G band decreases from 125.9 to 80.4 cm^{-1} with concomitant increase in the intensity of the peak. Finally, the G band peak position shifted from 1562 to 1586 cm^{-1} as the carbon was annealed

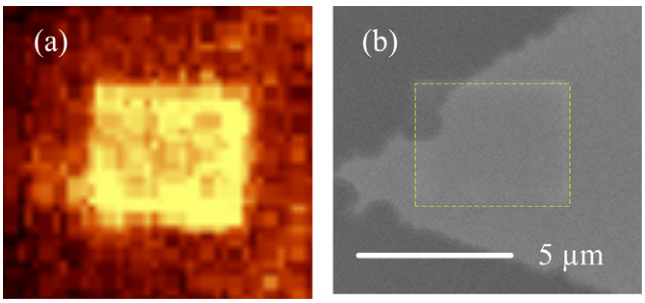

Figure 10. (a) Confocal Raman map of an EBID-made carbon square acquired by integrating the area under the spectra from 1500 to 1700 cm^{-1} (b) corresponding SEM image.

at elevated temperatures. The decrease of the D/G band ratio and the narrowing of the G band and the shift of the G band to higher wavenumbers clearly suggest the conversion of sp^3 bonds to sp^2 bonds, removal of hydrogen, and conversion of amorphous carbon to crystalline graphite materials, all significantly affecting contact resistance discussed above [12].

5. Conclusions

The effect of EBID-made carbon joint geometry, material properties, and phase composition on the total resistance of MWNT interconnects is systematically investigated. EBID carbon joints are fabricated using Quanta 200 ESEM with residual hydrocarbons as a precursor. The influence of the EBID-made carbon joints on the electrical resistance of the MWNT-to-metal interconnects is measured using two approaches. First, the electric current resulting from a DC electric potential difference imposed across the metal electrodes bridged by a MWNT is measured *in situ* during the MWNT-to-metal electrode joint deposition process. Second, the deposition process is performed in several steps, and the steady-state current versus voltage measurements are collected ∼10 min after the end of each deposition stage. It is found that the electron beam contributes to the measured current through an interconnect in a direct and an indirect way. The direct contribution comes from the injected primary electrons and is found to be negligible. On the other hand, the numerous secondary electrons generated in the course of inelastic collisions of primary electrons as they scatter in the material during the deposition process alter the measured current significantly and must be accounted for avoid measurement artifacts. Specifically, turning on the electron beam significantly increases the measured current, while turning the beam off causes an exponential decay of the measured current. This behavior is consistent with an interpretation that the EBID-deposited material and the SiO_2 layer act as the capacitors for the electron beam generated electrons. As a result, the *in situ* current measurements during the deposition are intrinsically transient in nature, and in order to obtain the DC current versus voltage I–V curve for the MWNT–metal interconnect, the measurements have to be performed ∼10 min after the end of a deposition process as the system achieves a steady state.

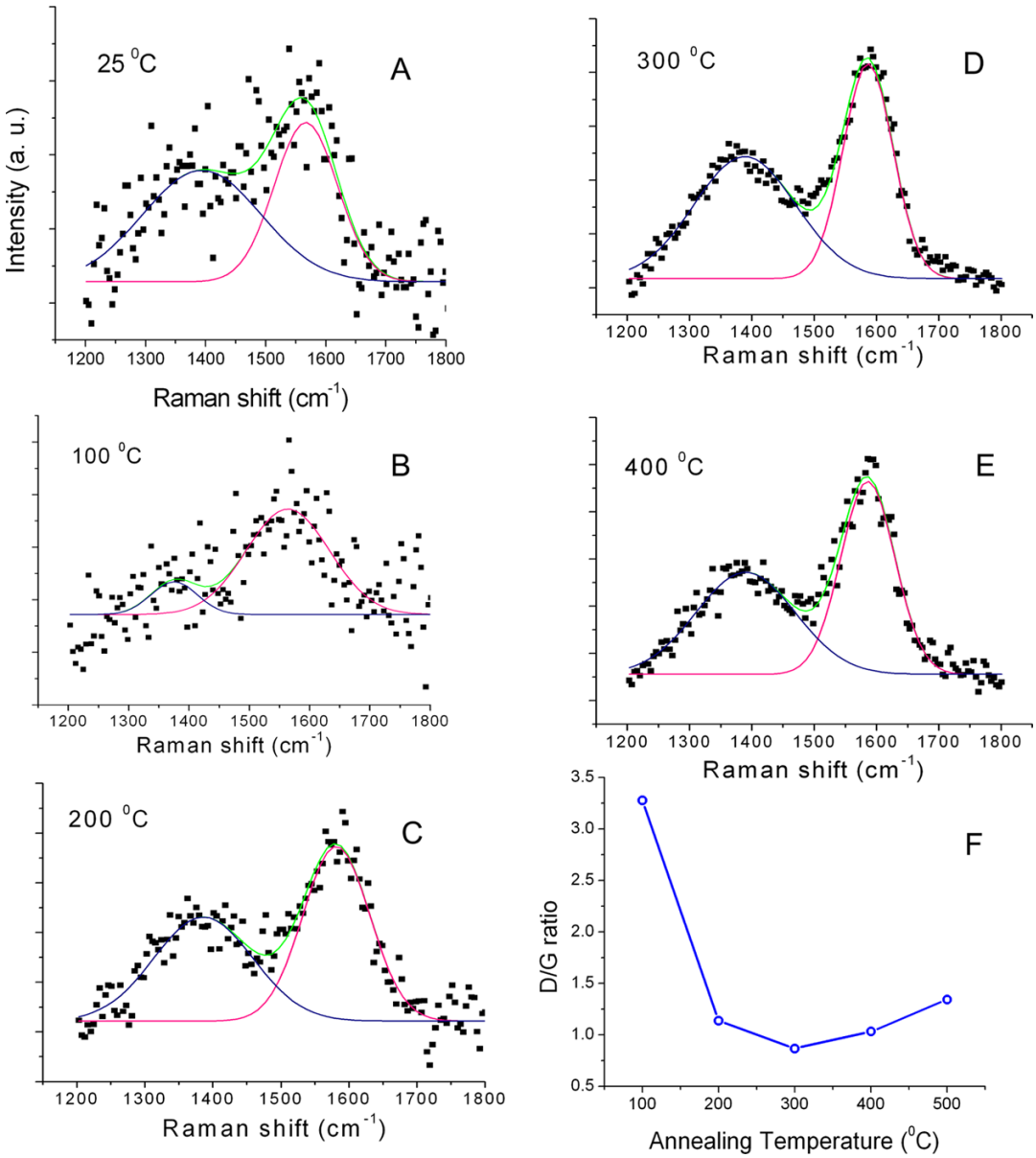

Figure 11. (A)–(E) Raman spectra (Gaussian fits) for EBID amorphous carbon squares annealed at different temperatures. The spectrum is deconvoluted into overlapping D and G band spectra. (F) Ratio of areas under the D and G bands as a function of temperature.

The cone-shape carbon joints connecting the MWNT and the metal electrode are fabricated using EBID with (20–30 keV and ∼5–140 pA) beam and a deposition time of 5 min. The *in situ* measured current is found to increase linearly with an increase in the cone base diameter. This trend is quantitatively confirmed using measurements of the total resistance of the MWNT interconnect, which is found to change proportionally to the inverse of the carbon joint diameter. Since the material phase composition and interfacial film properties remain the same during deposition experiments, only geometry of a deposited carbon joint (i.e., shape and dimensions) contribute to the lowering of the interconnect resistance. These results thus demonstrate the importance of topology of a MWNT-to-metal joint, and not only its material properties, on the overall electrical contact resistance of the MWNT-to-metal connection.

In order to assess an individual contribution of each geometric factor on the resistance of EBID-deposited carbon joints, deposition of EBID-made carbon square blocks is performed in different configurations. Comparison of the changes in the electric resistance with the corresponding changes in the relevant geometric scales of the deposits demonstrates that for EBID-made carbon joints $R_{\mathrm{aC-MWNTinterface}} \ll R_{\mathrm{aC}} + R_{\mathrm{aC-metalinterface}}$ and that a much smaller contact area between the carbon joint and a MWNT is needed as compared to that between the carbon joint and the metal pad/electrode.

Lastly, graphitization of amorphous carbon deposits is analyzed in response to the current induced Joule heating as well as thermal annealing via external heating. The resistance of the MWNT–metal interconnect is shown to decrease significantly upon phase transition in the EBID-made carbon joints forming the interface. It is found that the

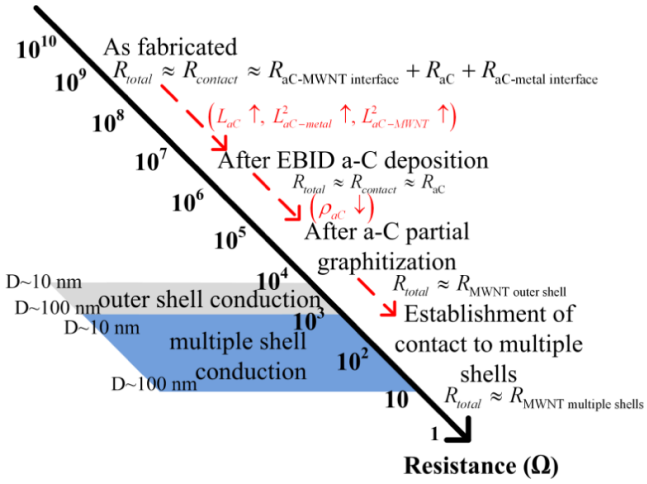

Figure 12. Chart summarizing the succession of dominant factors defining the total resistance of EBID-enabled MWNT interconnects and techniques that can be used for minimizing the magnitude of each resistance component (MWNT resistance values assume a 5 μm length of the tube).

resistivity of EBID carbon line decreases from 2×10^5 to 5×10^3 Ω μm during the Joule heating line experiments. The partial graphitization of EBID amorphous carbon due to thermal annealing is confirmed using Raman spectroscopy. Various features observed in the Raman spectra such as the decrease in the D/G ratio and the FWHM of the G band peak and the up shift of the G band peak position strongly support the graphitization of the EBID-made carbon upon annealing.

In summary, the analysis of different components contributing to the total joint resistance indicates that the bulk resistance of the carbon joint (R_{aC}) is ultimately the most dominant factor, and the bulk carbon resistivity ρ_{aC} can be reduced via annealing of the EBID-deposited carbon joint, As fabricated, the total resistance is the sum of the metal electrode–carbon joint interfacial resistance, carbon joint resistance, and the MWNT–carbon joint interfacial resistance. After deposition of a sufficiently large EBID amorphous carbon joint, the total resistance is limited solely by the resistance of the amorphous carbon material forming the bulk of the joint. Partial graphitization lowers the resistivity of the deposited amorphous carbon by two orders of magnitude. As shown in figure 12, after partial graphitization total resistance of the MWNT–metal interconnect is no longer limited by the contact resistance of the joint, but by the resistance of the outer shell of the MWNT. Further reduction in the total resistance of the MWNT interconnect can only be achieved through establishing an electrical contact to the inner shells of the MWNT.

Acknowledgments

Semiconductor Research Corporation (GRC Grant 2008OJ 1864.1281 managed by Dan Herr) and NSF Grant DMI 0403671 provided financial support for this work.

References

[1] Ajayan P M, Schadler L S, Giannaris C and Rubio A 2000 Single-walled carbon nanotube–polymer composites: strength and weakness *Adv. Mater.* **12** 750
[2] Anantram M P and Leonard F 2006 Physics of carbon nanotube electronic devices *Rep. Prog. Phys.* **69** 507–61
[3] Ando A, Shimizu T, Abe H, Nakayama Y and Tokumoto H 2004 Improvement of electrical contact at carbon nanotube/Pt by selective electron irradiation *Physica* E **24** 6–9
[4] Bachtold A, Henny M, Terrier C, Strunk C, Schonenberger C, Salvetat J P, Bonard J M and Forro L 1998 Contacting carbon nanotubes selectively with low-ohmic contacts for four-probe electric measurements *Appl. Phys. Lett.* **73** 274–6
[5] Banhart F 2001 The formation of a connection between carbon nanotubes in an electron beam *Nano Lett.* **1** 329–32
[6] Braunovic M 2006 *Electrical Contacts Fundamentals, Applications and Technology* (Boca Raton, FL: CRC Press)
[7] Bret T, Mauron S, Utke I and Hoffmann P 2005 Characterization of focused electron beam induced carbon deposits from organic precursors *Microelectron. Eng.* **78–9** 300-6
[8] Bret T, Utke I, Bachmann A and Hoffmann P 2003 *In situ* control of the focused-electron-beam-induced deposition process *Appl. Phys. Lett.* **83** 4005–7
[9] Brintlinger T, Fuhrer M S, Melngailis J, Utke I, Bret T, Perentes A, Hoffmann P, Abourida M and Doppelt P 2005 Electrodes for carbon nanotube devices by focused electron beam induced deposition of gold *J. Vac. Sci. Technol.* B **23** 3174–7
[10] Bussolotti F, D'Ortenzi L, Grossi V, Lozzi L, Santucci S and Passacantando M 2007 *In situ* manipulation and electrical characterization of multiwalled carbon nanotubes by using nanomanipulators under scanning electron microscopy *Phys. Rev.* B **76** 125415
[11] Choi Y R, Rack P D, Frost B and Joy D C 2007 Effect of electron beam-induced deposition and etching under bias *Scanning* **29** 171–6
[12] Chu P K and Li L H 2006 Characterization of amorphous and nanocrystalline carbon films *Mater. Chem. Phys.* **96** 253–77
[13] Close G F, Yasuda S, Paul R, Fujita S and Wong P H S 2008 A 1 GHz integrated circuit with carbon nanotube interconnects and silicon transistors *Nano Lett.* **8** 706–9
[14] Ding W, Dikin D A, Chen X, Piner R D, Ruoff R S, Zussman E, Wang X and Li X 2005 Mechanics of hydrogenated amorphous carbon deposits from electron-beam-induced deposition of a paraffin precursor *J. Appl. Phys.* **98** 014905
[15] Dockendorf C P R, Steinlin M, Poulikakos D and Choi T Y 2007 Individual carbon nanotube soldering with gold nanoink deposition *Appl. Phys. Lett.* **90** 193116
[16] Dong L F, Youkey S, Bush J, Jiao J, Dubin V M and Chebiam R V 2007 Effects of local Joule heating on the reduction of contact resistance between carbon nanotubes and metal electrodes *J. Appl. Phys.* **101** 024320
[17] Ferrari A C and Robertson J 2000 Interpretation of Raman spectra of disordered and amorphous carbon *Phys. Rev.* B **61** 14095–107
[18] Frank S, Poncharal P, Wang Z L and de Heer W A 1998 Carbon nanotube quantum resistors *Science* **280** 1744–6
[19] Gazzadi G C and Frabboni S 2009 Structural evolution and graphitization of metallorganic–Pt suspended nanowires under high-current-density electrical test *Appl. Phys. Lett.* **94** 3
[20] Graham A P *et al* 2005 How do carbon nanotubes fit into the semiconductor roadmap? *Appl. Phys.* A **80** 1141–51
[21] Jiang C Y, Ko H Y and Tsukruk V V 2005 Strain-sensitive Raman modes of carbon nanotubes in deflecting freely suspended nanomembranes *Adv. Mater.* **17** 2127

[22] Jiang J, Dong J M, Yang H T and Xing D Y 2001 Universal expression for localization length in metallic carbon nanotubes *Phys. Rev.* B **6404** 4
[23] Kahng Y H, Choi J, Park B C, Kim D H, Choi J H, Lyou J and Ahn S J 2008 The role of an amorphous carbon layer on a multi-wall carbon nanotube attached atomic force microscope tip in making good electrical contact to a gold electrode *Nanotechnology* **19** 7
[24] Kennedy D P 1960 Spreading resistance in cylindrical semiconductor devices *J. Appl. Phys.* **31** 1490–7
[25] Ko H H, Pikus Y, Jiang C Y, Jauss A, Hollricher O and Tsukruk V V 2004 High-resolution Raman microscopy of curled carbon nanotubes *Appl. Phys. Lett.* **85** 2598–600
[26] Langford R M, Wang T X, Thornton M, Heidelberg A, Sheridan J G, Blau W and Leahy R 2006 Comparison of different methods to contact to nanowires *J. Vac. Sci. Technol.* B **24** 2306–11
[27] Li H, Yin W Y, Banerjee K and Mao J F 2008 Circuit modeling and performance analysis of multi-walled carbon nanotube interconnects *IEEE Trans. Electron Devices* **55** 1328–37
[28] Li H J, Lu W G, Li J J, Bai X D and Gu C Z 2005 Multichannel ballistic transport in multiwall carbon nanotubes *Phys. Rev. Lett.* **95** 086601
[29] Madsen D N, Molhave K, Mateiu R, Rasmussen A M, Brorson M, Jacobsen C J H and Boggild P 2003 Soldering of nanotubes onto microelectrodes *Nano Lett.* **3** 47–9
[30] Miura N, Ishii H, Shirakashi J, Yamada A and Konagai M 1997 Electron-beam-induced deposition of carbonaceous microstructures using scanning electron microscopy *Appl. Surf. Sci.* **114** 269–73
[31] Molhave K, Madsen D N, Dohn S and Boggild P 2004 Constructing, connecting and soldering nanostructures by environmental electron beam deposition *Nanotechnology* **15** 1047–53
[32] Molhave K, Madsen D N, Rasmussen A M, Carlsson A, Appel C C, Brorson M, Jacobsen C J H and Boggild P 2003 Solid gold nanostructures fabricated by electron beam deposition *Nano Lett.* **3** 1499–503
[33] Naeemi A, Sarvari R and Meindl J D 2005 Performance comparison between carbon nanotube and copper interconnects for gigascale integration (GSI) *IEEE Electron Device Lett.* **26** 84–6
[34] Nihei M, Kondo D, Kawabata A, Sato S, Shioya H, Sakaue M, Iwai T, Ohfuti M and Awano Y 2005 *Low-resistance Multi-Walled Carbon Nanotube Vias with Parallel Channel Conduction of Inner Shells: Proc. Interconnect Technology Conf. IEEE* (Burlingame, CA: Institute of Electrical and Electronics Engineers Computer Society) pp 234–6
[35] Porrati F, Sachser R and Huth M 2009 The transient electrical conductivity of W-based electron-beam-induced deposits during growth, irradiation and exposure to air *Nanotechnology* **20** 10
[36] Rao A M *et al* 1997 Diameter-selective Raman scattering from vibrational modes in carbon nanotubes *Science* **275** 187–91
[37] Reznik A, Richter V and Kalish R 1997 Kinetics of the conversion of broken diamond (sp(3)) bonds to graphitic (sp(2)) bonds *Phys. Rev.* B **56** 7930–4
[38] Rice P, Wallis T M, Russek S E and Kabos P 2007 Broadband electrical characterization of multiwalled carbon nanotubes and contacts *Nano Lett.* **7** 1086–90
[39] Sato S, Nihei M, Mimura A, Kawabata A, Kondo D, Shioya H, Iwai T, Mishima M, Ohfuti M and Awano Y 2006 *Novel Approach to Fabricating Carbon Nanotube via Interconnects Using Size-Controlled Catalyst Nanoparticles* (Burlingame, CA: IEEE) p 3
[40] Singamaneni S, Gupta M, Yang R S, Tomczak M M, Naik R R, Wang Z L and Tsukruk V V 2009 Nondestructive *in situ* identification of crystal orientation of anisotropic ZnO nanostructures *ACS Nano* **3** 2593–600
[41] Slade P G 1999 *Electrical Contacts: Principles and Applications* (New York: Dekker)
[42] Song J W, Lee J H, Seo H W and Han C S 2008 Characterization and air pressure sensing of doubly clamped multi-walled carbon nanotubes *Nanotechnology* **19** 4
[43] Subramanian A, Vikramaditya B, Dong L X, Bell D and Nelson B J 2005 Micro and nanorobotic assembly using dielectrophoresis *Robotics: Science and Systems I* (Cambridge, MA: Massachusetts Institute of Technology)
[44] Tamor M A and Vassell W C 1994 Raman fingerprinting of amorphous-carbon films *J. Appl. Phys.* **76** 3823–30
[45] Taylor D M 1981 Electron-beam-induced conductivity and related processes in insulating films *IEE Proc.* A **128** 174–82
[46] Tersoff J 1999 Contact resistance of carbon nanotubes *Appl. Phys. Lett.* **74** 2122–4
[47] Tuinstra F and Koenig J L 1970 Raman spectrum of graphite *J. Chem. Phys.* **53** 1126
[48] Wei X L, Liu Y, Chen Q and Peng L M 2008 Controlling electron-beam-induced carbon deposition on carbon nanotubes by Joule heating *Nanotechnology* **19** 5
[49] Yang L and Han J 2000 Electronic structure of deformed carbon nanotubes *Phys. Rev. Lett.* **85** 154–7
[50] Yoshikawa Y, Akita S and Nakayama Y 2007 Barrier modification at contacts between carbon nanotube and Pt electrode using well-controlled Joule heating *Japan. J. Appl. Phys.* 2 **46** L359–61